Analysis of Voltage Dip Impact on Doubly Fed Induction Generator under Dynamic Conditions

Kidist Berhane Zergaw[1], Milkias Berhanu Tuka[2*] iD

[1, 2] Electrical Power and Control Engineering Department, Adama Science and Technology University, Adama, Ethiopia

E-mail: mil_ber2000@astu.edu.et

Abstract— Doubly Fed Induction Generator (DFIG) is the most widely employed generator in the Wind Energy Conversion Systems (WECS) for the production of electricity. However, despite all of its various advantages, it is extremely vulnerable to grid faults such as voltage dip since its stator is directly coupled to the grid. A voltage dip problem is one the main issues among the power quality concerns. This fault causes the flow of excessive current across both the stator and the rotor terminals, which may lead to serious damage to the generator, power converters, and DC Link capacitor. On the other hand, the current Grid Codes (GC) requires the system to stay connected to the grid during this fault condition and support it in healing its nominal voltage. This capacity of the system is known as the Low Voltage Ride Through (LVRT) capacity. For the system to achieve such capacity, appropriate protection mechanisms or controlling strategies must be utilized. Therefore, in this paper, the crowbar protection technique, PI controller, and the Adaptive Neuro-Fuzzy Inference System (ANFIS) controller are employed. Furthermore, the performance of the system employing PI, crowbar, and ANFIS is analyzed and compared under grid fault conditions, i.e., a voltage dip with a magnitude of 0.1 pu (worst case) using MATLAB/Simulink software and based on actual data obtained from Adama II wind farm. The obtained results unveil that the settling time of ANFIS for controlling the rotor currents in d and q axes (idr and iqr) and DC link voltage is 3.6 s, 3.57 s, and 3.4 s, respectively. On the other hand, the settling times of the PI controller for controlling the rotor currents in d and q axes and the DC link voltage are found to be 4 s, 3.91 s, and 45.2 s, respectively, while the crowbar protection technique's settling times are found to be 4 s, 6 s, and 4.9 s, respectively. It is evident from the aforesaid results that the ANFIS controller provides the best performance of the three strategies since it allows both the rotor currents and the DC link voltage to return to their steady state values faster than the other two techniques, employed in this investigation.

Keywords— Voltage dip; Adaptive neuro-fuzzy inference system; Crowbar; Doubly fed induction generator; Low voltage ride through.

1.   INTRODUCTION

Nowadays, more focus is being given to renewable energy sources (RES) mainly due to the developing environmental issues associated with the usage of traditional energy sources [1]. Among the different RES, wind energy is the most rapidly expanding source of electricity nowadays [2]. Wind Turbines (WTs) can be classified as variable or fixed-speed wind turbines depending on the speed of the rotor. For several reasons, a variable-speed wind turbine is becoming more advantageous than a fixed-speed wind turbine. The ability to generate a large amount of energy over a wide range of wind speeds, the reduction of acoustic noise, power fluctuation reduction, and the ability to control power independently are just a few of its advantages [3]. Among different variable-speed wind turbines, the

Doubly Fed Induction Generators (DFIG) shown in the Fig. 1 is widely used for the production of electrical energy [4], where GSC stands for the Grid Side Converter and MSC is for Machine Side Converter.

This is due to its wide-range operation speeds and converters having lower power ratings. As a result, the converter's overall cost and losses are reduced [5]. However, despite all of its advantages, DFIG-based WECS is extremely sensitive to grid faults, particularly for voltage dips. This is mainly due to the direct coupling of the stator of the generator to the grid and also due to the limited capacity of converters. Voltage dips in a weak grid will generate undesirable dynamics in the controller of DFIG-based wind turbines, possibly resulting in signal instability [6]. Furthermore, it may also cause rotor overcurrent and DC link fluctuation, which leads to some serious damage to semiconductors used in the Rotor Side Converter (RSC) as well as on the DC link capacitor. However, despite all this, the current Grid Code (GC) requires the system to remain coupled to the grid during this fault scenario and offer support to the grid to retain its nominal voltage within a short period, which is also known as Low Voltage Ride Through (LVRT) capacity. For the system to achieve such capacity, different protection techniques and control strategies must be employed [7, 8].
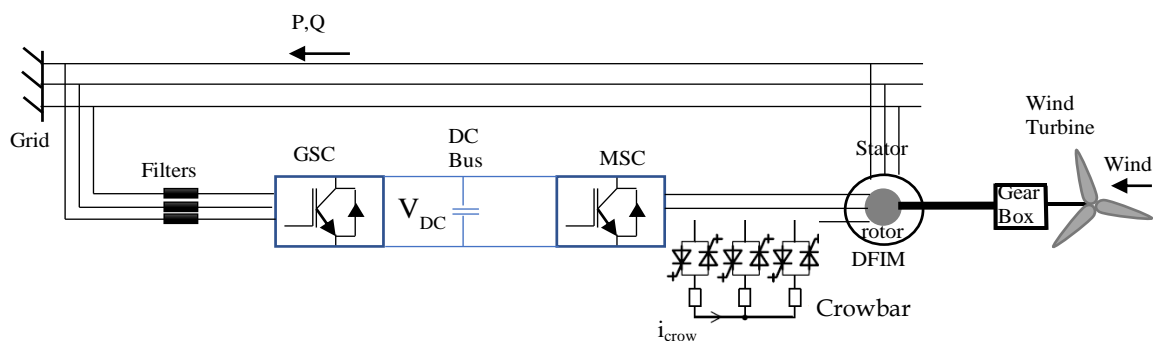

Fig. 1. DFIG based WECS.

Several studies have been conducted over the past few years to improve the LVRT capability of the DFIG wind turbine by utilizing various methods [9-14]. A variety of experiments have been carried out over the past years to enhance the LVRT capability of the DFIG wind turbine using different techniques. For instance, in [9], Crowbar is utilized to improve the system's LVRT capability. A crowbar is a bank of resistors that are connected between the DFIG's rotor and the Rotor Side Converter as shown in Fig. 1. In this paper, asymmetrical faults such as LG and LLG faults are taken into consideration. The results show that the DC link voltage is effectively suppressed, and also by setting the crowbar resistance to 1, the massive rotor current can pass through it. As a result, the rotor current keeps its nominal value after a fault. However, since the RSC is blocked during the crowbar operation, power loss occurs, and the fault generates large transients, which could lead to the system being isolated from the grid. In addition to this, when the crowbar is activated, the DFIG transforms into a conventional squirrel-cage induction generator (SCIG), absorbing a considerable amount of reactive power from the grid and delaying the grid voltage recovery process. Another drawback of utilizing a crowbar is that the value of its resistance should be sufficiently high to limit the rotor current effectively, but the high value of this resistance produces a high voltage drop in the rotor circuit.

In [10], the performance of the proposed technique during symmetrical and asymmetrical faults is evaluated by using PSCAD/EMTDC software. The results demonstrate that by employing a modified DC chopper with sufficient resistance, both the stator and rotor currents are maintained within their limits without the need for any extra voltage sag compensation techniques or fault current limiting techniques. In comparison to a crowbar, DC chopper, or a DC chopper and a crowbar, this approach is better since it enables the system to function in both fault current limiting and DC link voltage control modes. It also allows the grid to recover its nominal voltage within a short period since the RSC is not blocked during its action. However, the usage of additional switches for current limiting purposes creates harmonics in the system, resulting in some power quality issues. As a result, extra solutions are necessary to resolve this problem, increasing the system's cost. In addition to this, it also requires a properly designed chopper circuit; otherwise, it may cause some serious damage to the DC link capacitor.

In [11], the activity of shunt FACTS devices and advancements in LVRT ability improvement of DFIG-based WTs to keep up the voltage profile of the wind power generation are examined. The LVRT methods were compared based on their performance, the time taken for controller action, their cost, and augmented application reliability. It is concluded that because of its better voltage compensation and faster settling time than other shunt devices, STATCOM is the most effective and reliable in terms of LVRT capability enhancement.

In [14], the activity of FACTS devices and advancements for LVRT ability improvement of WTs is presented. The LVRT methods were compared based on their performance, complexity, their cost, and augmented application reliability and from the result obtained, it is concluded that DVR improves the system's LVRT capability better than the other series devices.

Although these final two arrangements are feasible in some instances, their applicability is limited due to the utilization of an auxiliary device, which makes the system more complex and more expensive.

In [15], the stator flux control technique of LVRT is tested on the 1.5 MW DFIG wind turbine during a symmetrical fault. In addition to this, the results obtained from simulating a system with and without the use of protective systems are compared. This technique is advantageous over the crowbar since it does not disable the RSC for protection purposes during the occurrence of a fault. Rather, it reduces the rotor current simply by attuning the flux and avoiding transient after the clearance of fault. However, creating torque fluctuation and inability of maintaining constant control that depends on the inductance of winding of DFIG during steady state operating conditions are some of the disadvantages of using this technique. To avoid such a problem, author of [13] uses an ANFIS controller to dampen the rotor overcurrent and DC link overvoltage during the fault period.

2. GRID CODE REQUIREMENTS

Most countries' grid codes attempt to ensure that their consumers have continuous access to electric power. This necessitates not only the appropriate level of generation to fulfil the load demand but also the capacity of users since both load and generation are responsible for ensuring the system's security. For this and related reasons, the following

critical technical criteria which may appear to be common across most countries due to their grid nature are necessary. These are [16, 17]:

- Fault ride-through capability
- Frequency and voltage tolerance
- Reactive power control and voltage support
- Active power control

3.   MODELLING OF DFIG

A Modelling of DFIG can start from the wind speed model which consists of four components, such as average, gust, ramp, and turbulence. The wind speed model can be obtained as follows [15, 18]:

$$V_w(t) = V_{wa}(t) + V_{wg}(t) + V_{wr}(t) + V_{wt}(t) \tag{1}$$

where $V_w(t)$ represents wind speed, $V_{wa}(t)$ represents average wind speed, $V_{wg}(t)$ represents the gust wind component, $V_{wt}(t)$ represents the turbulence component and $V_{wr}(t)$ represents ramp wind component, all in m/s.

Following the wind speed model, a wind turbine aerodynamic model can be established. In the wind turbine, aerodynamic model, power and torque are of its two main characteristics to be focused [14, 16]. With a wind speed of V_v, a wind disk radius of R, and a surface of A_1, the aerodynamic power of the wind, P_w is given by:

$$P_w = \frac{1}{2}\rho\pi R^2 V_v^3 \tag{2}$$

where ρ is the air density [kg/m³], R is the blade radius [m] and V_v is the wind speed [m/s].

The wind turbine's mechanical power, P_m, is calculated using the power coefficient C_p as follows:

$$P_m = Cp * P_w = \frac{1}{2}\rho\pi R^2 V_v 3 Cp(\lambda, \beta) \tag{3}$$

where C_p denotes the power coefficient, which indicates how well the WT captures wind energy and converts into mechanical energy. It can be expressed mathematically as follows:

$$Cp(\lambda, \beta) = C_1 * (\frac{C_2}{\lambda i} - C_3\beta - C_4\beta^{C_5} - C6) * \varepsilon^{-C_7/\lambda i} \tag{4}$$

and λ_i is given by:

$$\lambda_i = [\frac{1}{\lambda + C_8\beta} - \frac{C_9}{\beta^3 + 1}]^{-1} \tag{5}$$

where λ is the tip speed ratio, β represents the pitch angle, and C_1 to C_9 are the wind turbine's characteristic constants.

The ratio of the blade tip speed to the incoming speed is known as the tip speed ratio (TSR). It can be expressed mathematically as follows:

$$\lambda = \frac{\Omega * R}{Vv} \tag{6}$$

where Ω is the rotor's rotating angular speed and R is blade radius.

The aerodynamic torque is a ratio of mechanical power to the angular speed of the rotor. It can be obtained by:

$$T_m = \frac{1}{2}\rho\pi R^3 V_v^2 \frac{Cp(\lambda, \beta)}{\lambda} \tag{7}$$

The subsequent subsections describe the modelling approach of DFIG in WECS.

3.1. Modeling of DFIG in WECS

Due to the complexity of three-phase modeling, converting it to two-phase stationary, rotor, or synchronous frame of reference is desirable [19].

The voltage equations for the stator and rotors of the machine are given as follows:

$$V_{ds} = R_s i_{ds} + \frac{d\psi_{ds}}{dt} - \omega_s \psi_{qs}; V_{qs} = R_s i_{qs} + \frac{d\psi_{qs}}{dt} + \omega_s \psi_{ds}$$

$$V_{dr} = R_r i_{dr} + \frac{d\psi_{dr}}{dt} - \omega_r \psi_{qr}; V_{qr} = R_r i_{qr} + \frac{d\psi_{qr}}{dt} + \omega_r \psi_{dr}$$

(8)

The flux of the stator and rotor can be calculated using the following formulas:

$$\psi_{ds} = L_s i_{ds} + L_m i_{dr}; \psi_{qs} = L_s i_{qs} + L_m i_{qr}$$

$$\psi_{dr} = L_r i_{dr} + L_m i_{ds}; \psi_{qr} = L_r i_{qr} + L_m i_{qs}$$

(9)

where $L_s = L_m + L_{\sigma s}; L_r = L_m + L_{\sigma r}$

where V_{ds}, V_{qs}, V_{dr}, V_{qr} are voltages [V]; i_{ds}, i_{qs}, i_{dr}, i_{qr} are currents [A]; and $\psi_{ds}, \psi_{qs}, \psi_{dr}, \psi_{qr}$ are flux linkage [Wb] of the stator and rotor in the d and q axis, respectively.

The stator and rotor active and reactive power in the dq frame are computed as follows:

$$P_s = 1.5(V_{ds}i_{ds} + V_{qs}i_{qs}); Q_s = 1.5(V_{qs}i_{ds} - V_{ds}i_{qs})$$

$$P_r = 1.5(V_{dr}i_{dr} + V_{qr}i_{qr}); Q_r = 1.5(V_{qr}i_{dr} - V_{dr}i_{qr})$$

(10)

The electromagnetic torque equation is:

$$T_{em} = \frac{3}{2} p(\psi_{dr}i_{qs} - \psi_{qr}i_{ds}) = \frac{3}{2} pLm(i_{dr}i_{qs} - i_{qr}i_{ds})$$

(11)

where p is the number of poles.

3.2. DC Link Modeling

This model describes the fluctuations in DC link capacitor voltage as a function of its input power [16].

The energy stored, W_{dc}, is given by:

$$W_{dc} = \int P_{dc} dt = \frac{1}{2} C V_{dc}^2$$

(12)

where P_{dc} is the DC link's input power, V_{dc} is the voltage at the DC link, and C is the capacitance of the capacitor.

The input power to DC link can be calculated as:

$$P_{dc} = P_{in} - P_c = \frac{dW_{dc}}{dt}$$

(13)

where P_{in} refers to the RSC's input power and P_c represents the GSC's output power.

The DC link voltage, V_{bus}, is given by:

$$V_{bus} = \frac{1}{C_{bus}} \int i_c dt$$

(14)

where C_{bus} is the DC link capacitance and i_c is the current through capacitor.

The following equation is used to obtain the current through the capacitor:

$$i_c = i_{r\_dc} - i_{g\_dc} - i_{res} \qquad (15)$$

where i_{g_dc} denotes direct current flowing from the DC link to the grid [A], i_{r_dc} denotes direct current that flows from the rotor to the DC link [A], and i_{res} is current in the resistor [A].

On the other hand, the rotor and grid direct currents can be calculated as follows:

$$i_{r\_dc} = -s_{a\_r} i_{ar} - s_{b\_r} i_{br} - s_{c\_r} i_{cr}$$

$$i_{g\_dc} = s_{a\_g} i_{ag} + s_{b\_g} i_{bg} + s_{c\_g} i_{cg} \qquad (16)$$

where Sa_g, Sb_g, and Sc_g are GSC's switch signals and Sa_r, Sb_r, and Sc_r are RSC's switch signals.

The following equation is used to obtain the current flow through the resistor along with the DC link model shown in Fig. 2.
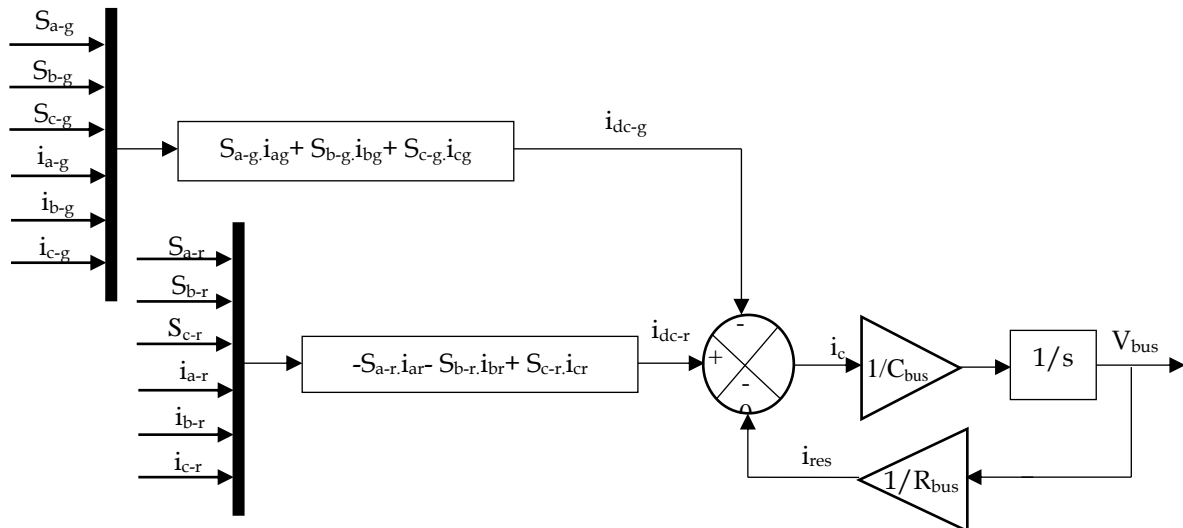
$$i_{res} = \frac{V_{bus}}{R_{bus}} \qquad (17)$$

Fig. 2. DC link model [16].

4.   ANFIS CONTROLLER

An ANFIS controller is a Sugeno fuzzy inference neural network that integrates the reasoning ability of Fuzzy Logic Controller (FLC) and the learning capability of a Neural Network (NN) into a single frame of work. In such a way, it reduces the time it takes to determine these ranges and rules and also provides optimized results [20]. The structure of the network is composed of five interconnected layers [21]. Fig. 3 depicts the single-input, single-output ANFIS structure.

Layer 1: Fuzzification Layer
It is a layer where the Membership Function (MF) of input is obtained. It is an adaptive layer whose output is given by:

$$O_i^1 = \mu_{Ai}(e) \quad \text{where i=1, 2,..m} \qquad (18)$$

where e is an error (input), A_i is the linguistic variable and μ is the membership function.

There are several types of membership functions. Among those, in this paper, triangular-based MF is selected since it is more popular and simpler to design than the others. It can be expressed as:

$$\mu_{A_i}(e) = trimf(e, ai, bi, ci) \tag{19}$$

$$\mu_{A_i}(e) = \max(\min(\frac{e-ai}{bi-ai}, \frac{ci-e}{ci-ai}), 0) \ ,i=1,2,\ldots m \tag{20}$$

where ai, bi, and ci are premises or antecedent parameters.

Layer 2: Rule Layer

It is a fixed layer whose output is the firing strength (weight) of the rule. It multiplies the incoming inputs and provides output for the next layer. However, in this case, since only one input is used the output from this layer will be the same as the first layer. It can be represented as:

$$O_i^2 = \mu_{A_i}(e) \tag{21}$$

Layer 3: Normalization Layer

It is also a fixed layer whose output is normalized firing strength (weight) of the rule obtained from layer 2. It is the ratio of the weight of each node to the total weight. It is given by:

$$O_i^3 = \overline{wi} = \frac{wi}{\sum_i wi} \ , i=1, 2, \ldots m \tag{22}$$

Layer 4: Defuzzification Layer

It is an adaptive layer that takes the normalized weight as an input and provides a consequent parameter set. It can be obtained as:

$$O_i^4 = \overline{wi} * fi = \overline{wi}(ki * e + ri) \ ,i=1, 2, \ldots m \tag{23}$$

where ki and ri are consequent or output parameters.

A Least Square Method (LSM) which is a form of mathematical regression analysis is utilized to determine the consequent parameters on the fourth layer in order to determine the line of best fit after training.

Layer 5: Output Layer

It is a fixed layer whose output is obtained by the summation of incoming signals. It can be expressed as follows:

$$O_i^5 = \sum_i \overline{wi} * fi = \frac{\sum_i wi * fi}{\sum_i wi} \ , i=1, 2, \ldots m \tag{24}$$

As previously stated, layers 1 and 4 are adaptive layers whose value at each node is changed with the error so that the optimized relation between the input and output is obtained. This can be done by proper tuning of the premise and consequent parameters. Therefore, to archive this, in this paper, hybrid algorism is employed for training purposes. It is a combination of the LSM and Back Propagation (BP). While the LSM is utilized to determine the consequent parameters on the fourth layer, on the other hand, BP is used to

reduce the error and to make the model more reliable. This is archived by propagating the error backward and tuning the premise parameters [22]. In this paper, the ANFIS controller is employed to control the DC link voltage and rotor currents with its structure as in Fig. 3.
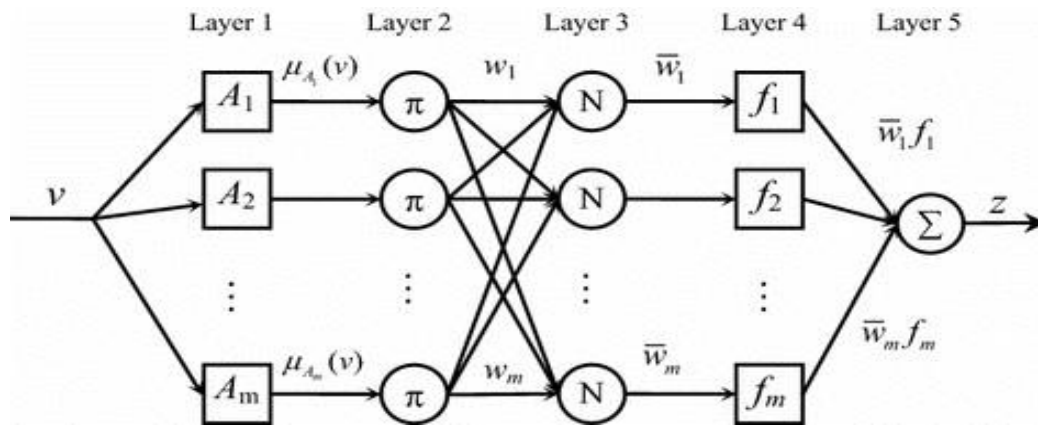

Fig. 3. ANFIS structure [22].

There are some steps that need to be followed while designing this controller in MATLAB-Simulink software. First, the training data (i.e., error and output) are generated from the PI controllers of the rotor currents as well as the DC link voltage and saved in the MATLAB's workspace. These data are arranged in the form of matrix in which the first column indicates the error and the last indicates the output. Then, these data are loaded into ANFIS GUI of MATLAB toolbox. Then the training is started after the selection of the type of MF for the inputs, the learning algorism and the number of iterations. In this paper, triangular MF and hybrid algorisms are selected. Triangular MF is selected for the inputs due to its simplicity and computational efficiency. On the other hand, the hybrid algorism, which is the combination of the Least Square Method and Back propagation, is used to obtain the consequent and premise parameters. Once the training is completed, the defuzzification process takes place and then fis file is extracted. Finally, this fis file is inserted and simulated in the MATLAB Simulink to obtain the required results (i.e., rotor currents and DC link voltage). Based on the parameters given in Table 1, the optimized architecture of the ANFIS and the obtained MF of premise parameter (i.e., error) are shown in Figs. 4 and 5, respectively.

Table 1. Parameters for the ANFIS structure.

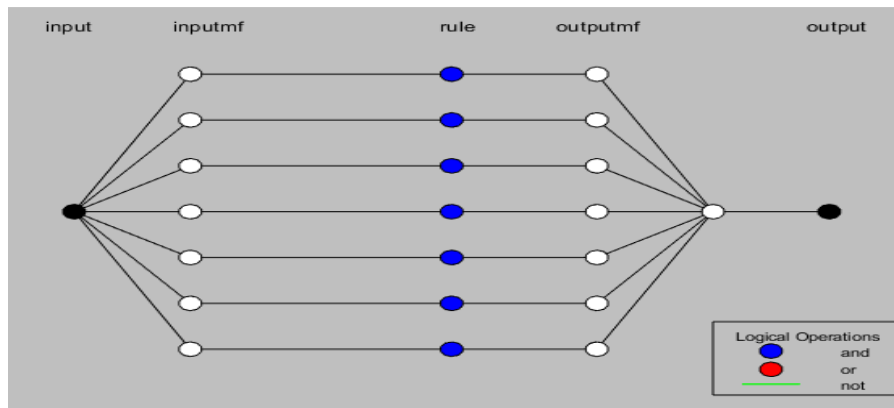| Parameter	Value
Number of inputs	1
Number of outputs	1
Number of rules	7
Number of epochs/ iterations	100
Total number of training data	250
Number of input MF	7
Types of input MF	Triangular
Number of output MF	7
Type of Inference system	Sugeno
Method	Hybrid

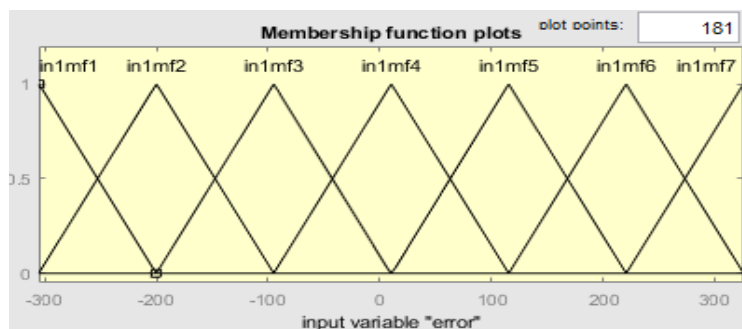Fig. 4. Optimized ANFIS structure.

Fig. 5. Membership function of error.

5. RESULTS AND DISCUSSIONS

The masked model of DFIG-based WECS is developed using MATLAB-Simulink 2021a as illustrated in Fig. 6. The WT, Generator, Converters, DC link, and Grid are the main components that are used while modeling this system. A DFIG with a power rating of 1.5 MW along with other parameters - obtained from Adama-II wind farm and exhibited in Table 2 – are employed.

Table 2. Adama-II generator and wind turbine parameters.

| Parameter	Value
Rated Power	1.5 MW
Rated Stator Line-to-Line Voltage	690 V
Rated Mechanical Torque	8292 N-m
Frequency	50 Hz
DC Link Voltage	1150 V
Number of Poles	2
Transformer Ratio	0.42
Gear Box Ratio	94.7
Cpmax	0.4865
Lambda Optimum	9
Inertia	67
Stator Winding Resistance	0.006243 Ω
Rotor Winding Resistance	0.011074 Ω
Stator Leakage Inductance	0.00008674 H
Rotor Leakage Inductance	0.0000723 H
Magnetizing Inductance	0.0055 H
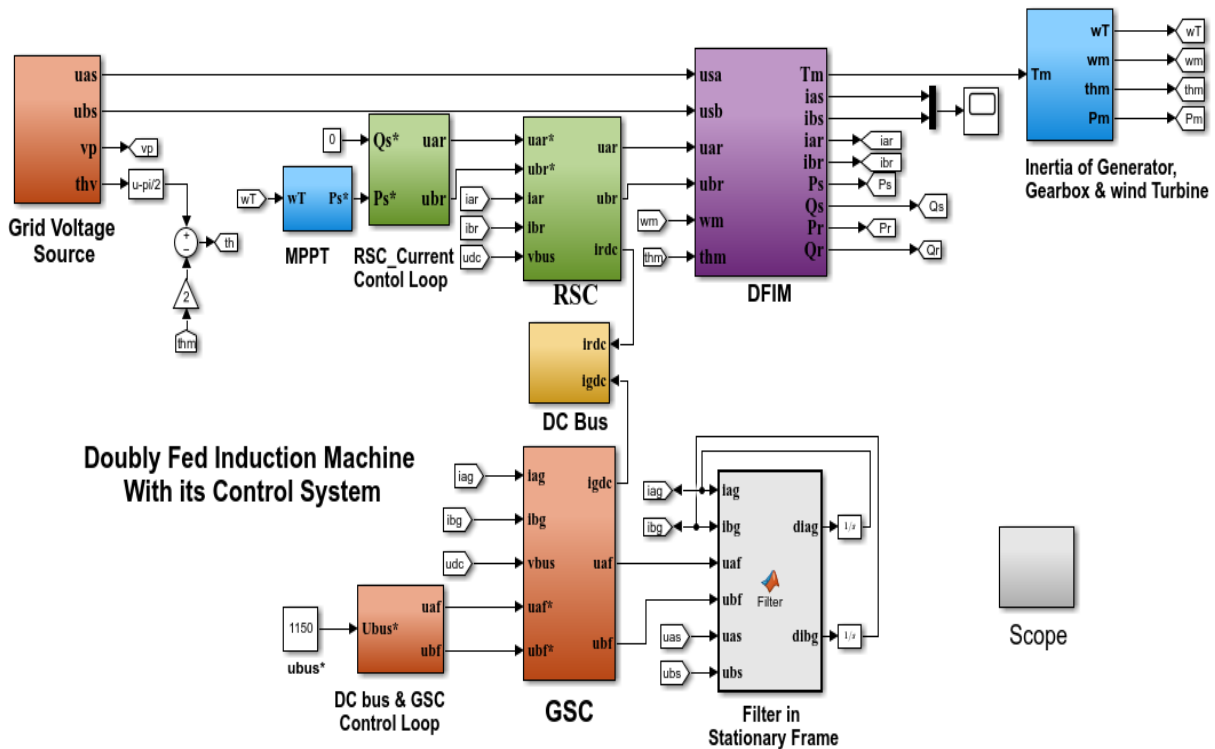
Fig. 6. Masked Matlab-Simulink model of the DFIG-based WECS.

In this section, the performance of the system under symmetrical fault conditions is analyzed by employing the PI controller, crowbar protection technique, and ANFIS controller as shown in Figs. 7, 8, and 9, respectively. To archive this, a voltage dip with a magnitude of 0.1 pu is applied at the third second of the simulation time. The analysis is done according to the German grid code requirement since it is the most suitable one for practical applications. For a voltage sag of 0.1 pu, the German grid code requires the wind turbine to remain connected to the grid for at least 150 ms and to maintain 90 percent of its nominal voltage within 1500 ms after the fault has been cleared [23, 24]. The impact of the fault on the steady-state operation of the system is shown in the following figures.

The stator voltage drops 90% of its normal value at the third second and continues to operate at this voltage for up to 3.15 s, as shown in Fig. 7 (a). However, it regained its nominal value after the complete clearance of the fault.

Figs. 7(b, c) depict the rise of current in the d and q-axis components of rotor current during a grid fault condition. However, both currents regained their nominal values after the fault is completely cleared from the system. Furthermore, when a voltage occurs across the grid terminal, the GSC loses control over the DC link voltage and it is also unable to transfer power to the grid. This led to the concentration of power at the DC link terminal charging the DC link's capacitor which subsequently causes overvoltage. The rise of DC link voltage during the fault period is shown in Fig. 7(d). However, it will start regaining its nominal value once the fault is completely cleared. On the other hand, the impact of this fault on the d and q-axis of grid current is illustrated in Figs. 7(e, f), respectively. Similar to that of the DC link voltage, these currents also start to follow their reference values after the complete clearance of the fault.
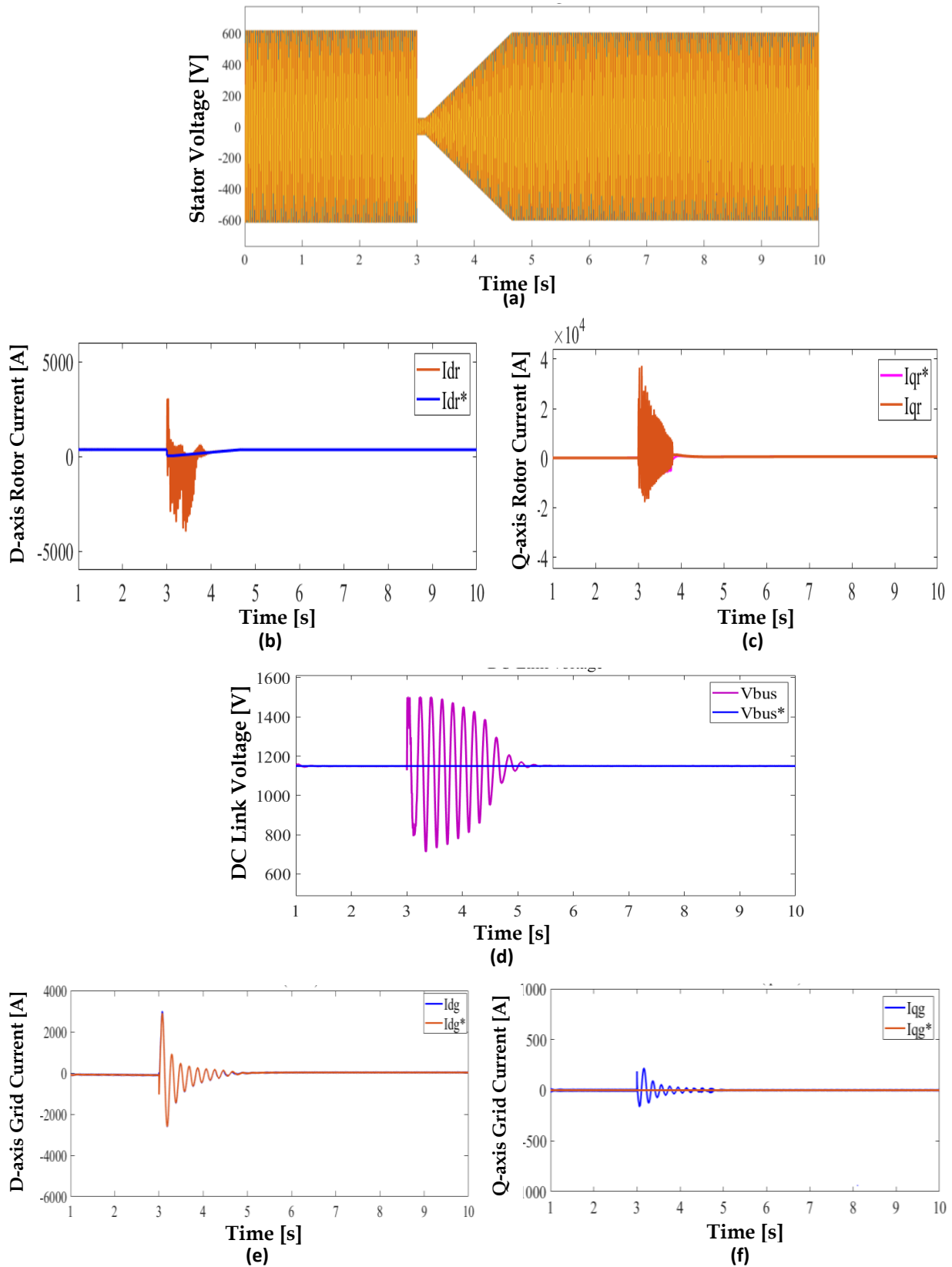
Fig. 7. LVRT improvement of DFIG using the PI controller: a) stator voltage; b) d-axis rotor current; c) q-axis rotor current; d) DC link voltage; e) d-axis grid current; f) q-axis grid current.

Fig. 8(a) shows that the stator voltage was operating at its steady state before the fault, but its magnitude was reduced when the fault has been occurred, and it continued the same

operation with this magnitude for the subsequent 150 ms. However, it returns to its normal operation at 1500 ms after the occurrence of the fault, as required by the German grid code. This is achieved because of the crowbar since it comes to operation by disabling RSC for 100 ms of voltage and protecting it from high currents appearing around the rotor winding during the fault. When the crowbar is disabled, the RSC again returns to its operational state, as shown in Fig. 8(b). The flow of a high amount of current across the direct and quadrature axis components of rotor current during this fault period are indicated in Figs. 8(c, d), respectively. However, once the fault has been completely cleared, all currents are returned to their pre-fault operation. During the crowbar operation, the RSC is unable to supply the generated power to the grid due to the fact that the voltage at the DC link terminal is decreased. However, once the fault is completely cleared, the DC link starts restoring its nominal voltage, as shown in Fig. 8(e). Similarly, the effect of this fault on the d and q-axis components of grid current is illustrated in Figs. 8(f, g), respectively.

When a symmetrical fault occurred at a grid terminal, the stator voltage dropped 90 % of its nominal value and continued to operate at this voltage magnitude, as shown in Fig. 9 (a). However, after 3.15 s, it started retaining its nominal value. Finally, after the complete clearance of the fault i.e, 3.65 s, it is returned to its steady state operation again as required by the German grid code. The rise in the d and q-axis components of rotor and grid currents during the fault period is shown in Fig. 9(b-f), respectively. However, these currents are returned to their normal operation once the fault is completely removed from the system. Finally, Fig. 9(d) shows that the DC link voltage is maintained at a steady state value with a few oscillations during the fault period.

6.   COMPARATIVE ANALYSIS

In this section, the performance of the system while employing the PI, crowbar, and ANFIS is compared and the conclusion is drawn based on the analysis.

6.1.   Comparison at Rotor Side Converter

In this sub-section, the parameters at the RSC are compared when PI, crowbar, and ANFIS are employed in the system. Fig. 10 illustrates different parameters in RSC for d-axis and q-axis. A distinct number is assigned to each figure to differentiate them from one another. The parameters with the PI controller, crowbar protection system and ANFIS controller for the rotor d-axis current are given are given by Figs. 10(a-c), respectively.

On the other hand, the results of the comparisons for the RSC for q-axis rotor current with PI, crowbar protection system and ANFIS controller are given by Figs. 11(a-c).

During the fault period, as shown in Figs. 10(a-c), a high amount of current flows in the d axis of the rotor terminal in all cases (PI, crowbar, and ANFIS). However, the system with ANFIS retains its nominal value within a short period compared to the remaining two techniques. In addition, it is also able to suppress a high amount of current flowing in the rotor terminal during the occurrence of a fault. In addition, similar to the d axis rotor current, the rotor current in the q axis also regains its nominal value when the fault is completely cleared, as shown in Figs. 11(a-c).

In addition to this, it is also observed that the system with ANFIS regains its nominal value within a short period compared to the others.
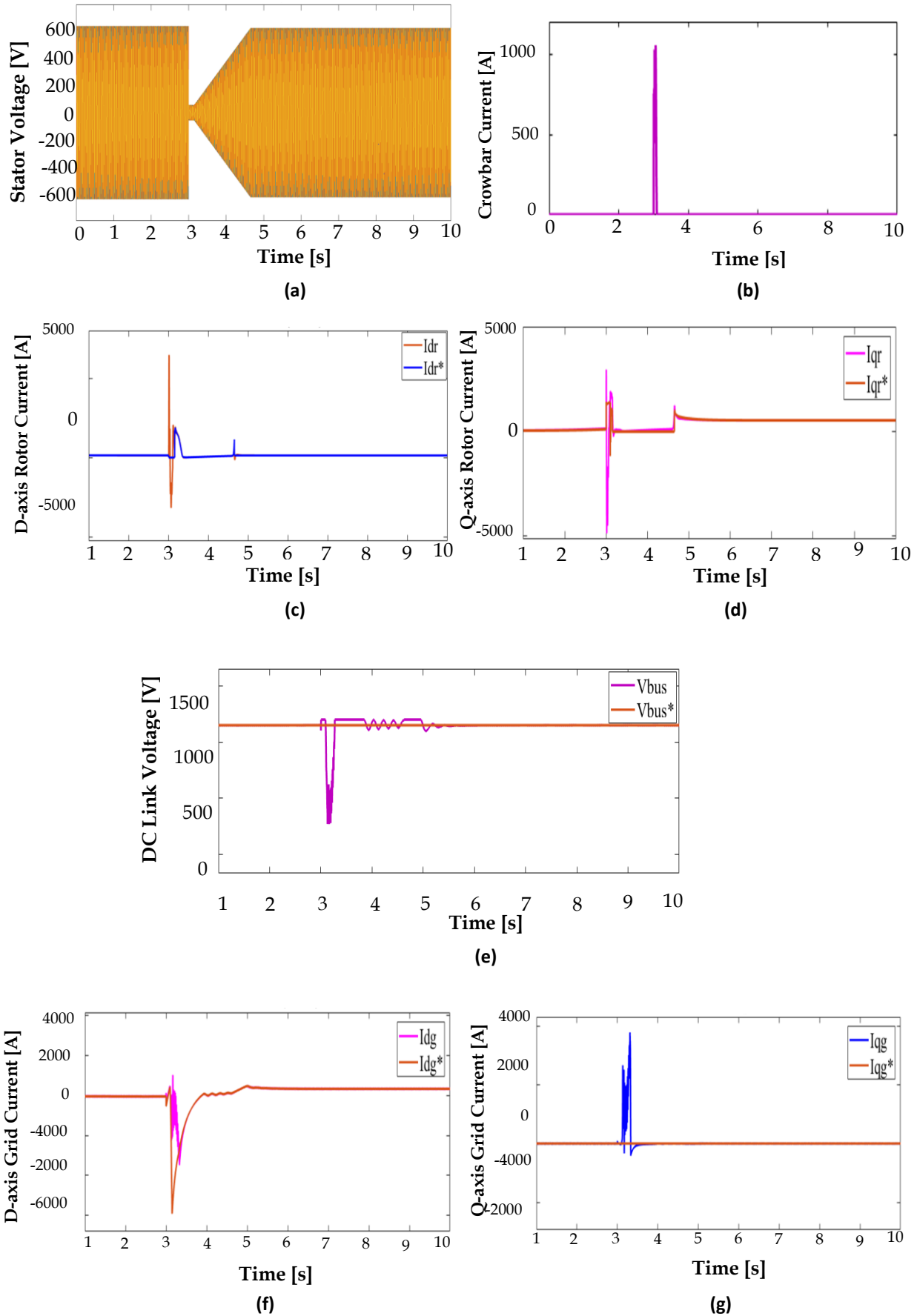
Fig. 8. LVRT improvement of the DFIG using the crowbar: a) stator voltage; b) crowbar current; c) d-axis rotor current; d) q-axis rotor current; e) DC link voltage; f) d-axis grid current; g) q-axis grid current.
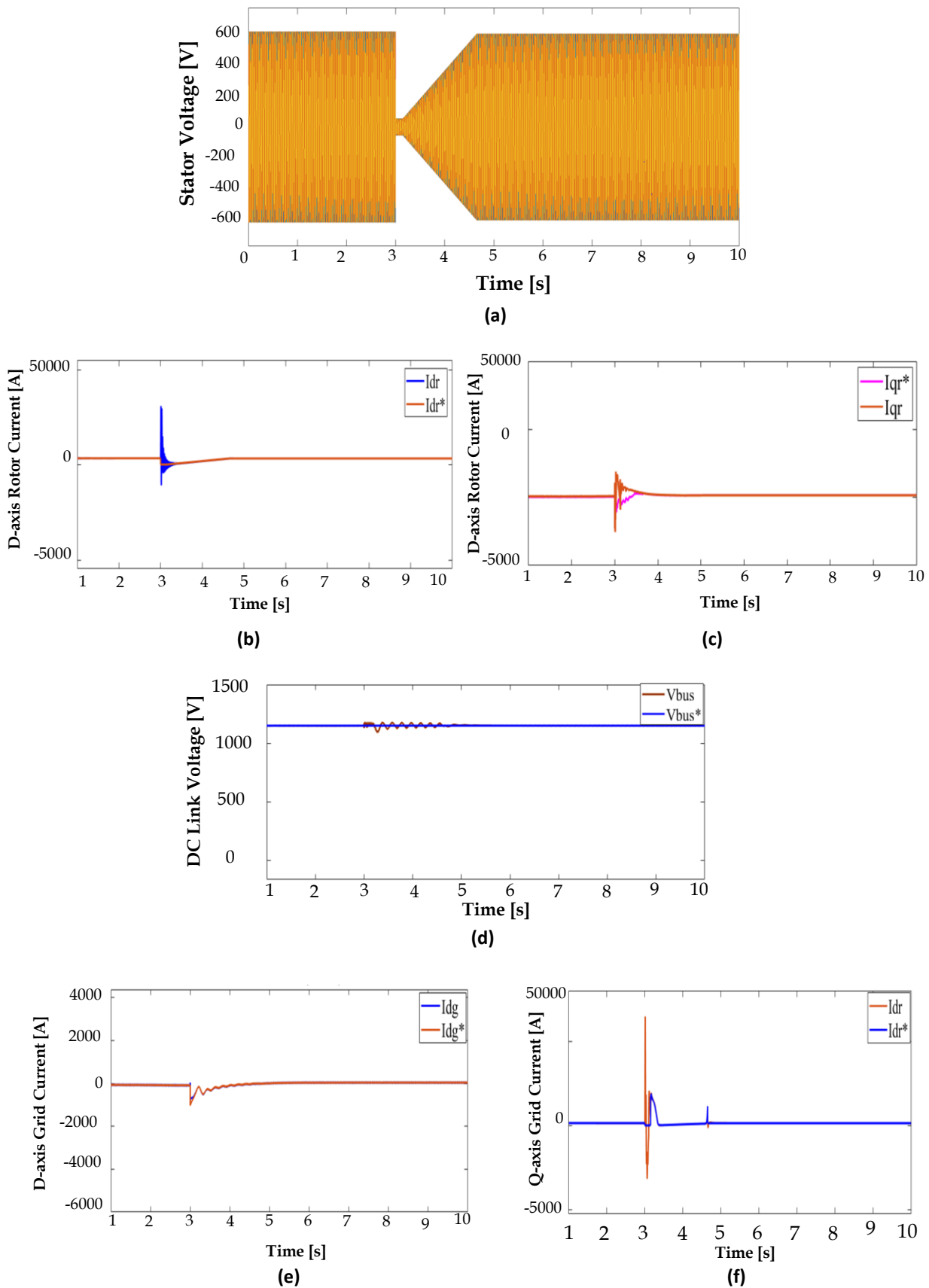
Fig. 9. LVRT improvement of the DFIG using the ANFIS controller: a) stator voltage; b) d-axis rotor current; c) q-axis rotor current; d) DC link voltage; e) d-axis grid current; f) q-axis grid current.
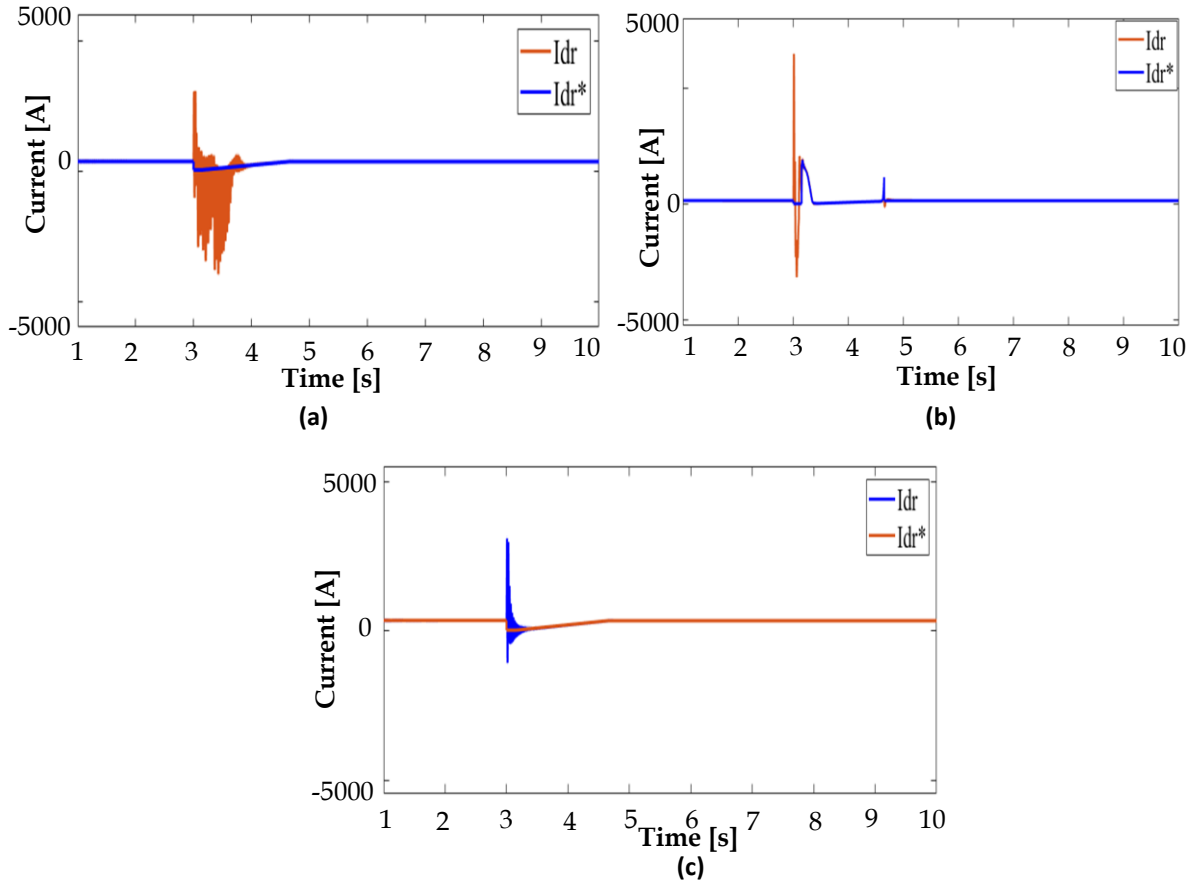
Fig. 10. D-axis rotor current at the RSC when employing the: a) PI; b) crowbar; c) ANFIS.
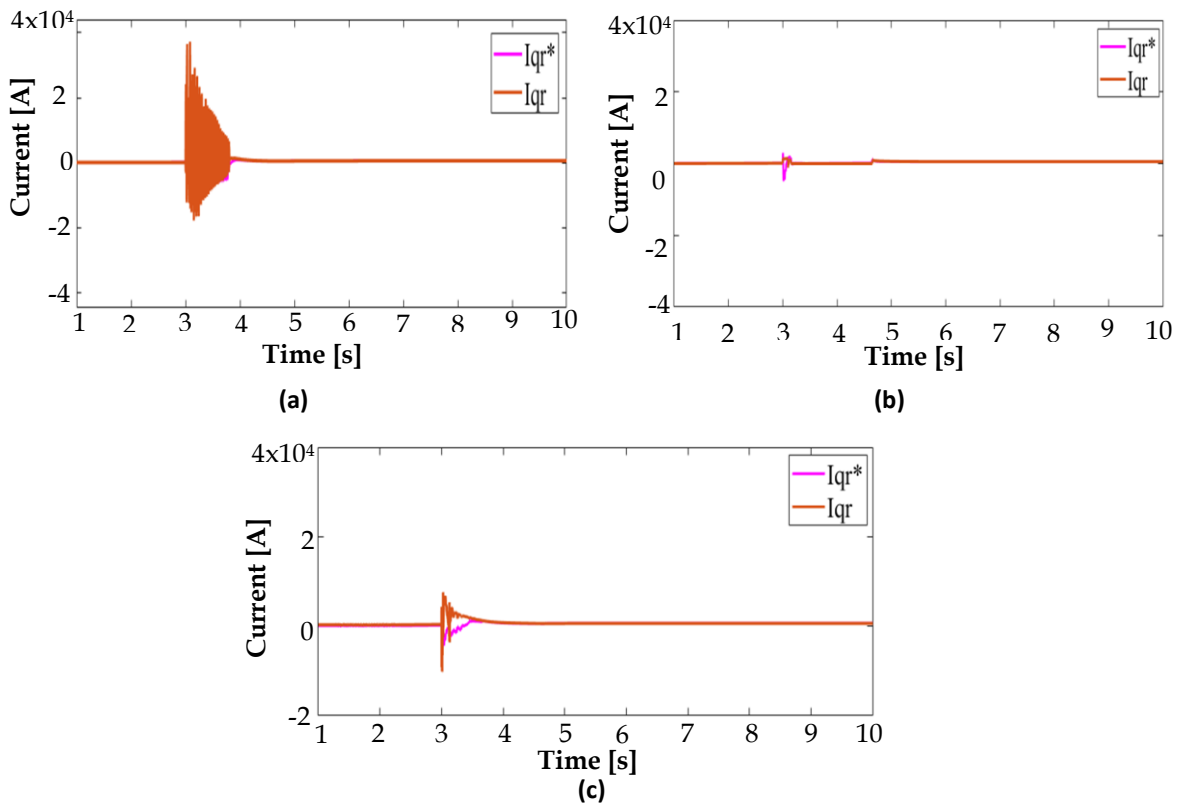

Fig. 11. Q-axis rotor current at the RSC when employing the: a) PI; b) crowbar; c) ANFIS.

6.2. Comparison at Grid Side Converter

In this sub-section, the parameters at the GSC are compared when PI, crowbar, and ANFIS are employed in the system. In this regard, Fig. 12 illustrates DC link voltage comparisons at GSC for the mentioned three cases respectively. In the same manner, Fig. 13 brings comparisons of d-axis grid current at GSC side.
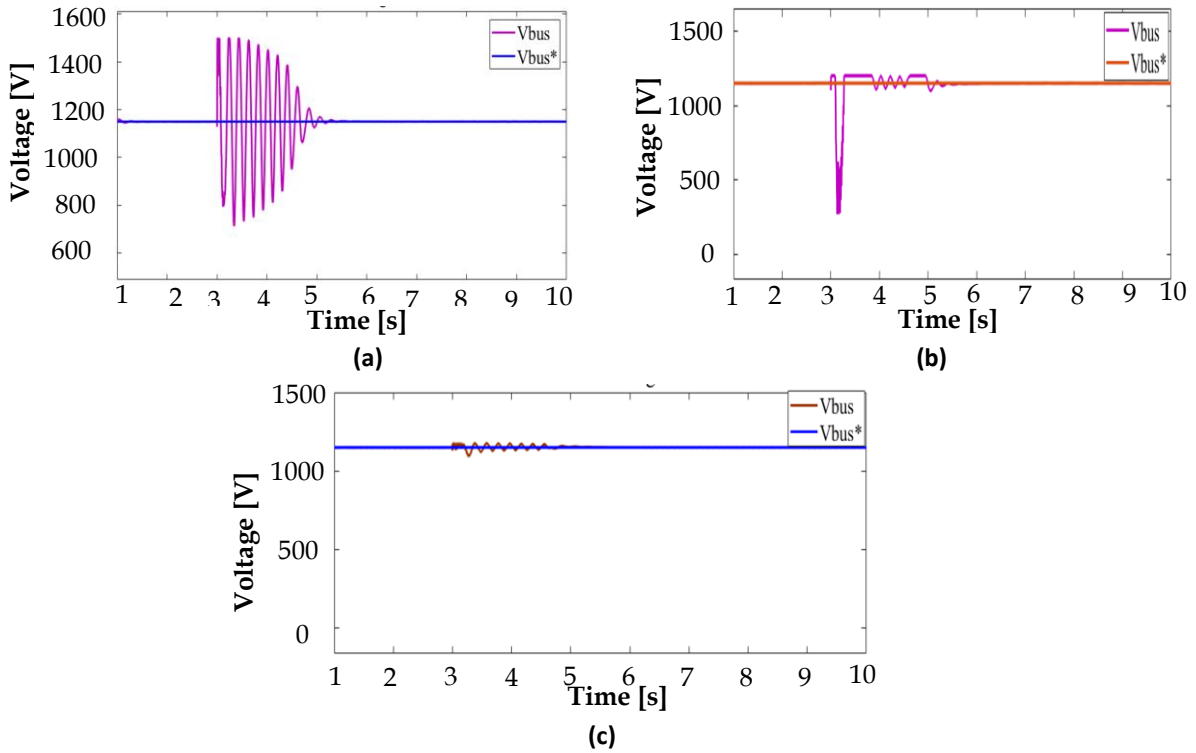

Fig. 12. DC link voltage at GSC when employing the: a) PI; b) crowbar; c) ANFIS.
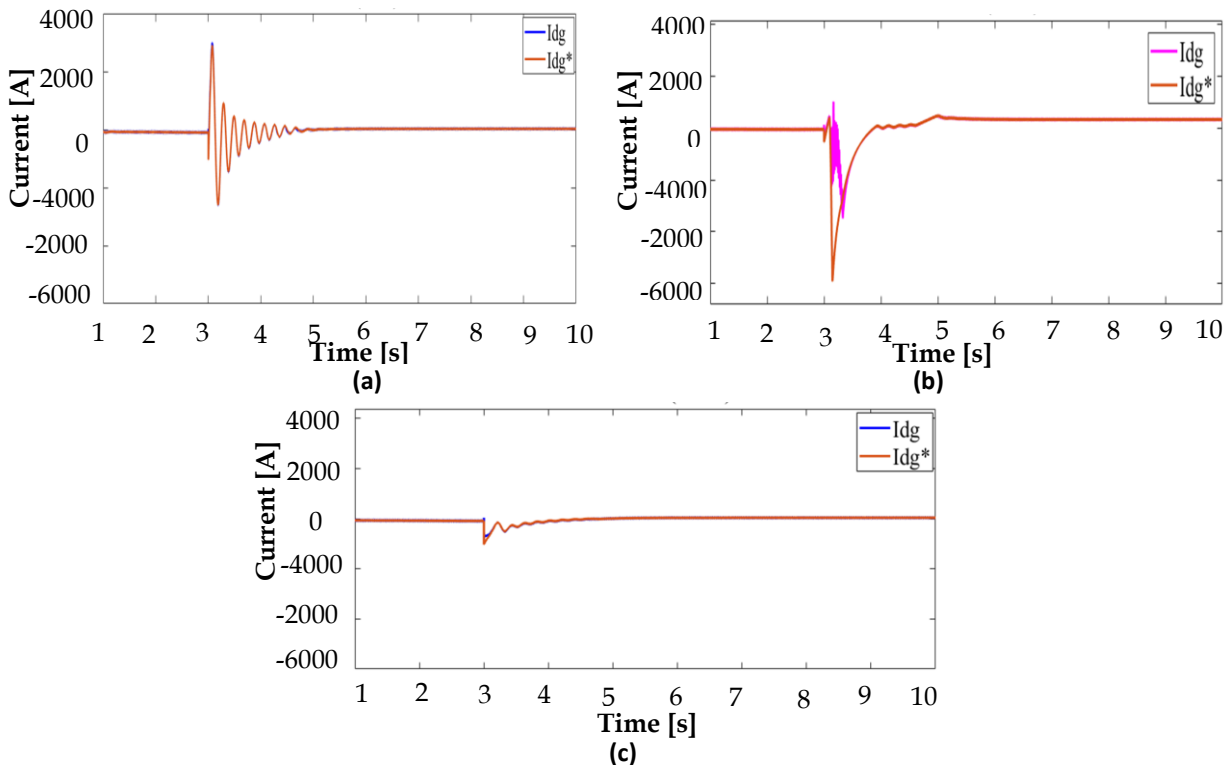

Fig. 13. D-axis grid current at GSC when employing the: a) PI; b) crowbar; c) ANFIS.

Finally, the results of the three comparative indexes for the case of q-axis grid current is depicted on Fig. 14 with PI, Crow bar protection system and ANFIS controllers.
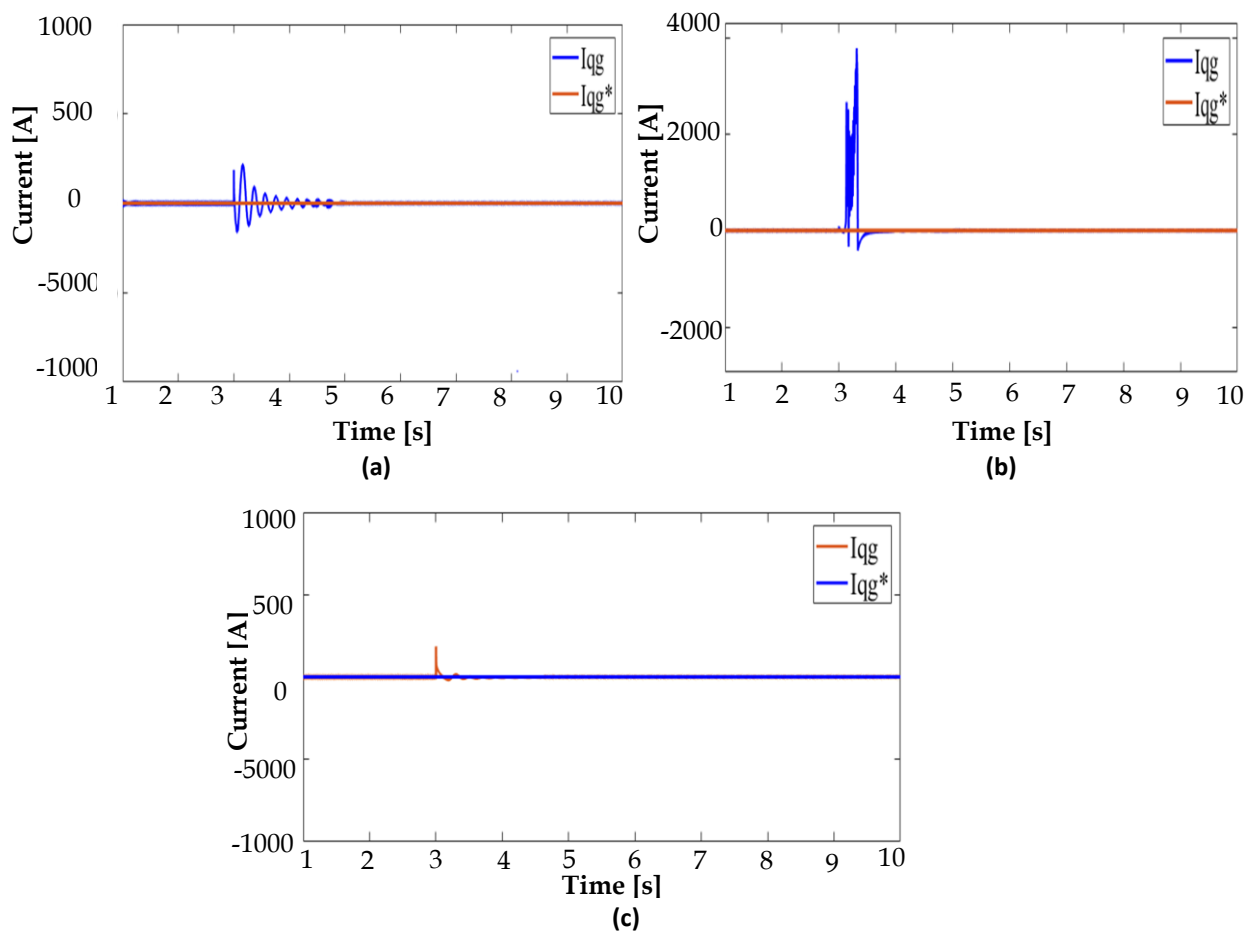

Fig. 14. Q-axis grid current at GSC when employing the: a) PI; b) crowbar; c) ANFIS.

Overall, comparison of the results obtained using the controllers and crowbars are shown in Table 3.

Table 3. Numerical comparison of RSC and GSC parameters with controllers.

Parameters		Settling time		
		PI Controller	Crowbar	ANFIS Controller
Rotor current	d axis	4 s	4.65 s	3.6 s
	q axis	3.91 s	4.65 s	3.57 s
Grid current	d axis	4.5 s	3.8 s	3.6 s
	q axis	5 s	4 s	3.4 s
DC-Link Voltage		5.2 s	4.9 s	3.4 s

7.   CONCLUSIONS

In this paper the performance of the DFIG under fault conditions i.e., voltage dip is analyzed. The crowbar protection technique and ANFIS controlling strategy are employed to improve the LVRT capacity of the system. Furthermore, the performance of the system using PI, crowbar, and ANFIS controller are compared. As previously stated, the LVRT capability

of the system is the ability of the system to stay connected to the grid when a voltage dip occurs on the grid terminals and support it to retain its nominal value within a short period. Based on the obtained simulation results, the system that employs the ANFIS controller performs better in protecting the system from damage and also in enhancing the LVRT capacity of the system than the other two techniques without disconnecting the RSC and also without employing any additional auxiliary devices. Therefore, we believe that the work will bring significant contribution towards DFIG under LVRT capability study in WECS.

REFERENCES

[1]   International Energy Agency, *Energy Statistics Course*, Paris, no. IEA, 2015.

[2]   A. Mengistu, "Analysis of dynamic voltage stability on the penetration of Adama II wind farm in Ethiopia grid," Addis Ababa University, 2017.

[3]   I. Haq, M. Khan, K. Zeb, "Siding mode control for PMSG based wind energy conversion system connected to the grid," *In 2016 International Conference on Computing, Electronic and Electrical Engineering*, pp. 277–282, 2016.

[4]   O. Al-Zabin, *Rotor Current Control Design for DFIG-Based Wind Turbine Using PI , FLC and Fuzzy PI Controllers*, Master Thesis, Rochester Institute of Technology, 2019.

[5]   V. Rao, K. Nanajee, "Dc-bus imbalance minimization for wind energy conversion system with five-level back-to-back converters using fuzzy logic," *International Journal of Industrial Electronics and Electrical Engineering*, vol. 4, no. 7, pp. 2347–6982, 2016.

[6]   J. Yang, J. Fletcher, J. O'Reilly, "A series-dynamic-resistor-based converter protection scheme for doubly-fed induction generator during various fault conditions," *IEEE Transactions on Energy Conversion*, vol. 25, no. 2, pp. 422–432, 2010.

[7]   C. Madan, N. Kumar, "Fuzzy grey wolf optimization for controlled low-voltage ride-through conditions in grid-connected wind turbine with doubly fed induction generator," *Simulation*, vol. 95, no. 4, pp. 327–338, 2019.

[8]   I. Hamdan, O. Noureldeen, "An overview of control method with various crowbar techniques of wind turbines during power system faults," *SVU-International Journal of Engineering Sciences and Applications*, vol. 2, no. 1, pp. 35–45, 2021.

[9]   P. Jayanthi, D. Devaraj, "Performance study of DFIG based grid connected WECS using crowbar and without crowbar," *In 2019 IEEE International Conference on Intelligent Techniques in Control, Optimization and Signal Processing*, pp. 1–3, 2019.

[10] S. Naderi, M. Negnevitsky, K. M. Muttaqi, "A modified DC chopper for limiting the fault current and controlling the DC-link voltage to enhance fault ride-through capability of doubly-fed induction-generator-based wind turbine," *IEEE Transactions on Industry Applications*, vol. 55, no. 2, pp. 2021–2032, 2019.

[11] B. Ganthia, "Shunt connected FACTS devices for LVRT capability enhancement in WECS," *Engineering, Technology & Applied Science Research*, vol. 10, no. 3, pp. 5819–5823, 2020.

[12] B. Ganthia, S. Barik, B. Nayak, "Low voltage ride through capability enhancement using series connected fact devices in wind energy conversion system," *Journal of Engineering Science and Technology*, vol. 16, no. 1, pp. 365–384, 2021.

[13] B. Naik, S. Naik, "ANFIS based control strategy for low voltage ride through capability in DFIG based wind farm," *International Journal of Scientific Research in Science and Technology*, vol. 3, no. 8, pp. 108–117, 2017.

[14] G. Abad, J. López, M. Rodríguez, L. Marroyo, G. Iwanski, *Doubly Fed Induction Machine: Modeling and Control for Wind Energy Generation*, John Wiley and Sons, 2011.

[15] R. Ibrahim, S. Watson, "Wind turbine simulation model for the study of combined mechanical and electrical faults," *European Wind Energy Association Conference*, no. November, 2015.

[16] M. Berhanu, Y. Mekonnen, R. Leidhold, M. Mamo, Z. Muluneh, A. Sarwat, "Analysis of a doubly fed induction generator through modeling and simulation," *In 2018 IEEE PES/IAS PowerAfrica*, pp. 652–657, 2018.

[17] Z. Li, H. Xu, Z. Wang, Q. Yan, ''Stability assessment and enhanced control of DFIG-based WTs during weak AC grid," *IEEE Access*, vol. 10, pp. 41371-41380, 2022.

[18] D. Rekioua, *Wind Power Electric Systems*, Green Energy and Technology, London Springer 2014.

[19] O. Janssens, N. Noppe, C. Devriendt, R. Van de Walle, S. Van Hoecke, "Data-driven multivariate power curve modeling of offshore wind turbines," *Engineering Applications of Artificial Intelligence*, vol. 55, pp. 331–338, 2016.

[20] V. Kumar, A. Pandey, S. Sinha, "Stability improvement of DFIG-based wind farm integrated power system using ANFIS controlled STATCOM," *Energies*, vol. 13, no. 18, pp. 1–18, 2020.

[21] B. Rezaie, S. Y. Nikoo, Z. Rahmani, "A novel intelligent fast terminal sliding mode control for a class of nonlinear systems: application to atomic force microscope," *International Journal of Dynamic Control*, vol. 6, no. 3, pp. 1335–1350, 2018.

[22] O. Noureldeen, I. Hamdan, "An efficient ANFIS crowbar protection for DFIG wind turbines during faults," *In 2017 Nineteenth International Middle East Power Systems Conference*, pp. 263–269, 2018.

[23] M. Mohseni, *Enhanced Control of DFIG-Based Wind Power Plants to Comply with the International Grid Codes*, Doctoral Dissertation, Curtin University, 2011.

[24] M. Tuka, "Investigation of voltage dip problems during faults on a grid-tied doubly fed induction generator in a wind energy system," *Jordan Journal of Electrical Engineering*, vol. 9, no. 2, pp. 209-227, 2023.